



Deposited via The University of Leeds.

White Rose Research Online URL for this paper:

<https://eprints.whiterose.ac.uk/id/eprint/183632/>

Version: Accepted Version

Article:

Fu, Z, Jin, H, Zhang, J et al. (2021) Air film evolution during droplet impact onto a solid surface. *Physics of Fluids*, 33 (9). 092107. ISSN: 1070-6631

<https://doi.org/10.1063/5.0063018>

© 2021 Author(s). This article may be downloaded for personal use only. Any other use requires prior permission of the author and AIP Publishing. The following article appeared in Zunru Fu, Haichuan Jin, Jun Zhang, Tianyou Xue, and Dongsheng Wen , "Air film evolution during droplet impact onto a solid surface", *Physics of Fluids* 33, 092107 (2021) and may be found at <https://doi.org/10.1063/5.0063018>. Uploaded in accordance with the publisher's self-archiving policy.

Reuse

Items deposited in White Rose Research Online are protected by copyright, with all rights reserved unless indicated otherwise. They may be downloaded and/or printed for private study, or other acts as permitted by national copyright laws. The publisher or other rights holders may allow further reproduction and re-use of the full text version. This is indicated by the licence information on the White Rose Research Online record for the item.

Takedown

If you consider content in White Rose Research Online to be in breach of UK law, please notify us by emailing eprints@whiterose.ac.uk including the URL of the record and the reason for the withdrawal request.

Air Film Evolution during Droplet Impact on a Solid Surface

Zunru Fu¹, Haichuan Jin¹, Jun Zhang¹, Tianyou Xue¹, Dongsheng Wen^{1,2}

¹ School of Aeronautic Science and Engineering, Beihang University, Beijing 100191, China

² School of Chemical and Process Engineering, University of Leeds, Leeds LS2 9JT, United Kingdom

Abstract

Recent years see increasing studies of air entrapment during droplet impacting on a solid surface but with inconsistent results. Accurate simulation of the evolvement of entrapped air film during a droplet impact on a solid surface was achieved in this work with phase field method by applying dynamic contact angle model. Based on the discusses about the effects of droplet viscosity and surface tension on the entrapped air film initial radius and its retraction dynamics, we discovered three regimes at later stage of contraction (Regime1: No daughter droplet-attachment; Regime2: Daughter droplet-attachment/detachment; Regime3: Daughter droplet-detachment) separated by Oh or an Oh_e number considering the lubrication effect of the air film. Under high Oh_e regime, the bubble tends to attach to the substrate because of no daughter generation as has been previously reported. However, under low Oh_e regime, the bubble tends to detach from the surface and a vortex street was found behind the retracting rim of the air volume which later produces a strong downstream flow inside the bubble that squeezes the daughter droplet out of the surrounding air. Under moderate Oh_e regime, the volume ratio between the daughter droplet and the bubble is apparently determined by the advancing contact angle after which the static contact angle determines whether the bubble will attach to or detach from the substrate. Our research finding provides better insight about controlling entrapped air bubble attachment/detachment behavior in droplet impacting on a solid surface.

1. Introduction

Droplet impact is a common phenomenon encountered in natural and industrial scenes such as ink-jet printing, spray cooling, aircraft icing and so on¹. When a droplet impacts on a solid surface it would always spread first and then may deposit, bounce or splash depending on the droplet properties, impact velocity, air components, surface wettability and surface roughness². Normally, impact dynamics is characterized by the Reynolds (Re), Weber (We), Ohnesorge (Oh), and Capillary (Ca) numbers, defined respectively as:

$$\text{Re} = \frac{\rho DU}{\mu} \quad \text{We} = \frac{\rho DU^2}{\sigma} \quad \text{Oh} = \frac{\sqrt{\text{We}}}{\text{Re}} = \frac{\mu}{\sqrt{\rho D \sigma}} \quad \text{Ca} = \frac{\mu U_{cl}}{\sigma}$$

where ρ is the liquid density, D is the droplet diameter, U is the impact velocity, μ is the liquid viscosity, σ is the surface tension and U_{cl} is the contact line moving speed.

Air entrapment is almost inevitable when a droplet impacts on a solid or a liquid surface in atmospheric environment. When a droplet comes close to the substrate, the lubrication pressure in the thin air layer beneath the droplet will deform the bottom surface of the droplet into a dimple shape, forming a ring-shaped contact to the surface. As soon as the spreading begins, a small volume of air gets entrapped beneath the droplet,

34 followed by a sequence of interface topological changes. Air entrapment is sometimes undesirable because it
35 would degrade ink-jet printing quality or reduce heat transfer in spray cooling for instance. Also, it has been
36 recently revealed that in an extreme low-pressure and high-humidity environment³, the compression from
37 entrapped air may modify the surface wettability due to water vapor condensation. For the fast-kinetic freezing
38 process of a droplet impacting on a supercooled solid substrate, a newly discovered type of delamination
39 behavior of the frozen splats was recently reported, where the entrapped bubble in the frozen splat acts as a
40 localized defect⁴.

41 Since Chandra and Avedisian⁵ firstly reported the air entrapment phenomenon during droplet impact in
42 1991, a few macroscopic studies have been conducted considering the initial air film size predictions, the air
43 film retraction dynamics modelling and the following contraction profiles description⁶⁻¹². Advances in
44 experimental methods, such as ultra-highspeed video camera photography⁶, dual wavelength interferometry¹³,
45 fast photography coupled with optical interference¹⁴ and total internal reflection (TIR) microscopy coupled
46 with virtual frame technique (VFT)¹⁵, have provided better visual insights both in time and in space, where
47 the influence of the surrounding air pressure, extreme high liquid viscosity, surface roughness and surface
48 elasticity have been studied¹⁶⁻²¹. However, the techniques such as light interference or total reflection tend to
49 lose some critical information when viewing from the bottom of the droplet, and can't reveal the bubble's
50 morphological changes in the vertical direction. A complete picture of air film dynamics and air film evolution
51 into a bubble [as shown in Fig.8](#) was successfully captured in 2012 by Lee from the front view using ultrafast
52 x-ray phase-contrast imaging²². Their study clearly showed that after the droplet impacting the surface in a
53 dimple shape of the bottom surface, a small volume of air was trapped beneath the droplet, forming an air film.
54 The air film would retract by surface tension to minimize the surface energy, while at the same time the
55 capillary wave on the upper surface would transport inward at a higher speed. As the wave reaches the
56 substrate, the air film would continue contracting and forming into a spherical bubble with a daughter droplet
57 entrapped inside. It was also found that at high Oh numbers, no daughter droplet was formed inside the final
58 spherical bubble because of the high viscous dissipation of the capillary wave. The static contact angle (SCA)
59 was suggested to play a decisive role on the attachment/detachment behavior of the bubble under moderate
60 Oh situation given that the volume ratio between the daughter droplet and the bubble, i.e., V_d/V_b , is
61 independent of SCA. However, it is still unclear what would happen at low Oh situation where the interfacial
62 force becomes dominant and also what determines the V_d/V_b value needs better understanding.

63 In parallel with experimental studies, some commonly used interface capture methods such as VOF,
64 CLSVOF, Lattice-Boltzmann have been used to show the formation of the air film, but with limited success
65 in capturing the subsequent dynamics, due to the large demand in computation source and the difficulties in
66 establishing surface tension on surfaces with complex microscale topological variations²³⁻²⁷. Most of the

67 existing simulation work mainly focuses on the deformation of the droplet before contact, the air pressure
68 distribution in the initial air film, the influence of the air film to the heat transfer between the liquid and the
69 wall, and the influence of the entrapped air to the liquid solidification process, few of them investigates the
70 following air film evolution dynamics. Recently, detailed dynamics of the air film upon a drop impacting
71 on a liquid pool was simulated by Jian with BASILISK codes²⁸, where three possible regimes were identified,
72 i.e., contracting into a single central bubble, forming a toroidal bubble, or splitting vertically into two smaller
73 bubbles. These regimes are separated by a newly proposed Oh_e number $Oh_e = OhSt^{-\frac{1}{3}}$ based on the air-film
74 thickness, St is the Stokes number and $St = \frac{\mu_g}{\rho DV}$ where μ_g is the gas viscosity. The study also revealed the
75 importance of vortex shedding at low Oh regime. For droplet impacting on a solid surface, it becomes more
76 complicated as the accurate boundary condition of the solid wall is difficult to be established. Very recently
77 Kumar studied air film evolution process and the influence of surface wettability to the
78 attachment/detachment of the air bubble using the VOF method²⁹. A critical SCA was found in differentiating
79 two regimes. The bubble would detach from the surface at $SCA < 35^\circ$ and would stay attached to the surface
80 at a high $SCA \sim (90^\circ - 120^\circ)$ ²⁶, which they claimed to correspond well with the experiment results of Lee²².
81 However, there are significant differences in between. According to Lee's experimental results, whether the
82 bubble would leave the surface happens apparently after the daughter droplet generation is finished. The
83 reason for bubble detachment could be explained by a geometrical relation, as shown in Fig.15²², that at a
84 given volume ratio V_d/V_b , the daughter droplet would spill out from the bottom of the bubble at a low SCA.
85 While in Kumar's simulation, the detachment happens before the toroidal bubble convergence. It is believed
86 that the use of SCA model in Kumar's simulation is inappropriate as the air film retraction speed could reach
87 5 m/s ^{6, 22}, leading to a large Ca number of 0.068. This suggests that the movement of the contact line should
88 be better described by the dynamic contact angle (DCA) rather than the SCA.

89 In order to advance the understanding of air film dynamics upon a droplet impacting on a solid surface,
90 a detailed numerical study was conducted based on the Phase Field Method (PFM) in combination with a
91 DCA model in this work. The DCA model is established experimentally by capturing the droplet dynamics in
92 analogy to the entrapped air evolution. After successfully validated by the Lee's experiments, the effects of
93 droplet viscosity and surface tension on the dynamics of the air bubble are studied, and three possible regimes,
94 including one that has never been reported, are identified depending on the Oh or the Oh_e number. The detailed
95 mechanisms of air film dynamics are further examined by the energy conversion and flow field analysis.

96 **2. Simulation and experimental section**

97 **2.1 Phase Field Method**

98 Phase Field Method (PFM) is an interface tracking method for two-phase flow dynamics based on Cahn-

Hilliard diffuse theory³⁰ coupling with the Navier–Stokes equation. It has gained quite a lot attention since Yue³¹, and has been successfully applied in many multiphase simulation work³²⁻³⁷. It is particularly useful when there is rapid spatial change in the micro-scale topology of the fluid interfaces or when the interface thickness is comparable to the length scale of the system, where the sharp-interface methods such as VOF could not capture accurately the interfacial curvature. The PFM is adopted in this work.

In the PFM, the diffuse interface is defined as the region where the dimensionless phase field variable ϕ goes from 0 to 1, and the Cahn-Hilliard equation is split up into two equations:

$$\begin{aligned} & \frac{\partial \phi}{\partial t} + \mathbf{u} \cdot \nabla \phi \\ & = \nabla \cdot \frac{\gamma \delta}{\varepsilon^2} \nabla \Psi, \end{aligned} \quad (1)$$

Ψ

$$= -\nabla \cdot \varepsilon^2 \nabla \phi + (\phi^2 - 1)\phi. \quad (2)$$

where \mathbf{u} is the fluid velocity field, $\gamma = \chi \varepsilon^2$ is the mobility parameter (χ is defined as the mobility tuning parameter), δ is the mixing energy density, and ε is the interface thickness parameter. The following equation relates the mixing energy density and the interface thickness to the surface tension coefficient:

$$\sigma = \frac{2\sqrt{2}}{3} \frac{\delta}{\varepsilon}.$$

In the phase field interface, the volume fractions of the individual fluids are:

$$V_{f1} = \frac{1-\phi}{2},$$

$$V_{f2} = \frac{1+\phi}{2}.$$

The density ρ and the viscosity μ of the mixture vary smoothly over the interface as:

$$\rho = \rho_1 + (\rho_2 - \rho_1)V_{f2},$$

$$\mu = \mu_1 + (\mu_2 - \mu_1)V_{f2}.$$

The transport of mass and momentum in phase field method is governed by the Navier-Stokes equations with surface tension incorporated in the model to better simulate capillary effects:

$$\begin{aligned} & \rho \frac{\partial \mathbf{u}}{\partial t} + (\mathbf{u} \cdot \nabla) \mathbf{u} \\ & = \nabla \cdot [-p\mathbf{I} + \mu(\nabla \mathbf{u} + (\nabla \mathbf{u})^T) + \mathbf{F}_{st} + \rho \mathbf{g}], \end{aligned} \quad (3)$$

$$\nabla \cdot \mathbf{u} = 0.$$

\mathbf{F}_{st} is the surface tension:

$$\mathbf{F}_{st} = G \nabla \phi.$$

And G is chemical potential:

$$G = \delta \left[-\nabla^2 \phi + \frac{\phi(\phi^2 - 1)}{\varepsilon^2} \right].$$

As seen above, the phase field surface tension is computed as a distributed force over the interface using

only the gradient of the phase field variable. This computation avoids using surface curvature, which may be troublesome to represent numerically.

Normally two dimensionless numbers are important in phase field method:

(1) **Cahn number** $Cn = \frac{\varepsilon}{L}$: relative thickness of the interface compared with the system length scale.

(2) **Péclet number** $Pe = \frac{LU\varepsilon}{\gamma\sigma} = \frac{LU}{\chi\varepsilon\sigma}$: relative strength of advection over the diffusion of the fluid components at the interfacial region, where L is the characteristic length (such as the droplet diameter D before impact) and U is the characteristic velocity (such as the droplet impact velocity). $Cn \sim 0.01$ has been previously verified as a proper choice to achieve satisfactory precision without costing too much computing resource³¹⁻³⁵. While the phenomenological mobility parameter γ or the mobility tuning parameter χ , which determines the time scale of the Cahn-Hilliard diffusion, must be chosen judiciously. It must be sufficiently large to retain a constant interfacial thickness but small enough so that the convective terms are not overly damped. It has been recently proved by Bai³⁷ that the mobility parameter γ and the Pe should be kept as a constant for a given physical system and thus Pe is proportional to the interface thickness ε when χ and other physical properties are fixed.

Wall and contact angle boundary force is defined as:

$$\mathbf{u} \cdot \mathbf{n}_{\text{wall}} = 0,$$

$$\mathbf{F}_\theta = \sigma \delta(\mathbf{n}_{\text{wall}} \cdot \mathbf{n} - \cos\theta_w) \mathbf{n}. \quad (4)$$

where θ_w is the contact angle of the surface, and δ equals a Dirac delta function that is nonzero only at the fluid interface. The method allows to specific the contact angle with a small amount of slip, the slip boundary sets the velocity component normal to the wall to zero as:

$$\mathbf{u} \cdot \mathbf{n}_{\text{wall}} = 0.$$

and adds a frictional force \mathbf{F}_c as:

$$\mathbf{F}_c = \frac{\mu}{L_s} \mathbf{u}.$$

where L_s is slip length.

2.2 Model Description

A two-dimensional axisymmetric model is established, as seen in Fig 3, where a water droplet of diameter $D_0 = 2.6 \text{ mm}$ impacts onto a solid surface at a velocity of $U_0 = 1.25 \text{ m/s}$, corresponding to Lee's experiments²². The size of the domain is $2D_0 \times 1.5D_0$. The density of $\rho = 996.4 \text{ kg/m}^3$, the dynamic viscosity of $\mu_0 = 1.005 \text{ mPa}\cdot\text{s}$ and the surface tension between the droplet and the air of $\sigma_0 = 7.275 \times 10^{-2} \text{ N/m}$ are used for the water droplet. The air pressure of the gas phase as well as the upper and side pressure boundary conditions are all set as $P_0 = 1 \text{ atm}$. For the wall boundary a slip boundary condition is used to capture the effect of the DCA model.

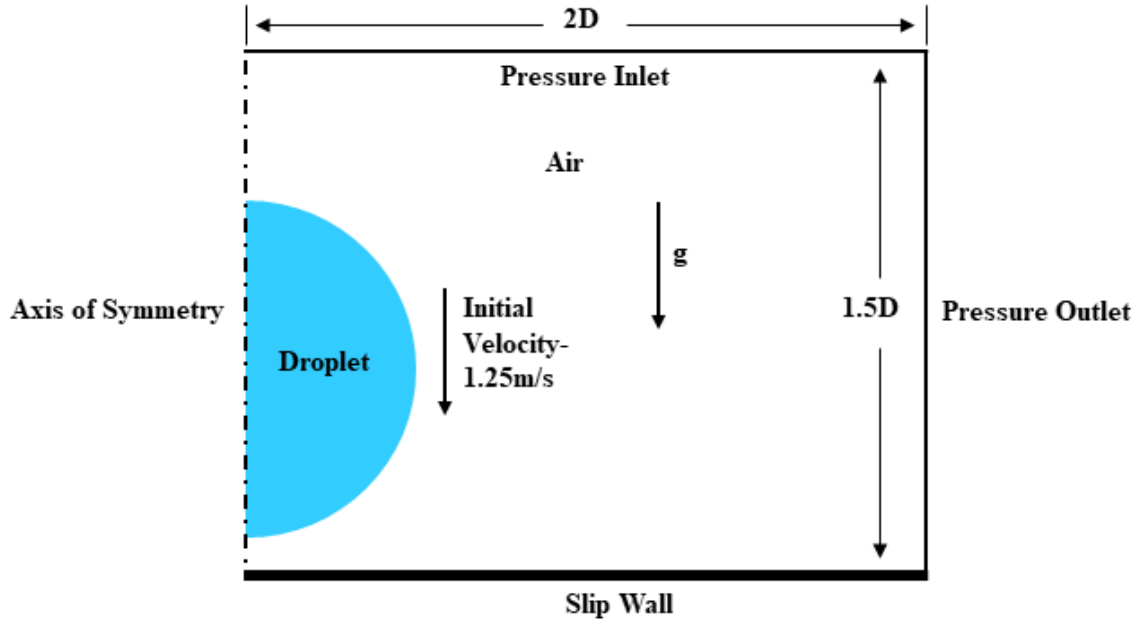


Figure 1 Sketch of the simulation model

2.3 Dynamic Contact Angle (DCA) Model

DCA model is quite important in simulating droplet impact dynamics, where the movement of the triple contact line and the apparent contact angle are not governed by the interface energy properties described by Young's Equation³⁸. For example, the initial rapid contact line spreading of an impacting droplet is dominated by inertia; however as it reaches the maximum spreading diameter with the inertia vanished, its later behavior is more controlled by the interactions between the surface tension and the viscous force^{38, 39}. The DCA is mainly influenced by the droplet diameter and impact velocity, which is a result of the competitions among the inertia³⁹⁻⁴¹, the viscosity of the droplet³⁹⁻⁴², the wettability of the substrate⁴⁰⁻⁴⁴ and the liquid-gas surface tension^{40, 41, 43, 44}. The DCA has been shown to capture well the droplet impact dynamics such as the maximum spreading diameter coefficient, up to the point of splashing threshold^{42, 45, 46}. Although it's still not understood clearly, it is generally agreed that the DCA is a function of the contact line movement speed^{38, 47}. In 2008, Yokoi etc. proposed a DCA model⁴⁸ based on the Tanner's law:

$$Ca = k(\theta_d - \theta_e)$$

for capillary-dominated situation (low Ca number), where Ca is the capillary number and k is a material related constant that is empirically determined, θ_d is the dynamic contact angle, θ_e is the equilibrium contact angle. For inertia-dominated situation (high Ca number), the approximation is taken as:

$$\theta_d = \begin{cases} \theta_a, & U_{cl} \geq 0 \\ \theta_r, & U_{cl} \leq 0 \end{cases}$$

where θ_a is the maximum advancing contact angle and θ_r is the minimum receding contact angle. So, the Yokoi dynamic contact angle model can be written as:

$$\theta_d(U_{cl}) = \begin{cases} \min \left[\theta_e + \left(\frac{Ca}{k_a} \right)^{\frac{1}{3}}, \theta_a \right], & U_{cl} \geq 0 \\ \max \left[\theta_e + \left(\frac{Ca}{k_r} \right)^{\frac{1}{3}}, \theta_r \right], & U_{cl} \leq 0 \end{cases} \quad (5)$$

2.4 Dynamic Contact Angle Measurement

It is quite hard to measure the DCA inside a droplet during the air film evolution, but it would be much easier to capture from the outer droplet spreading-receding process. The DCA is determined by the contact line movement, influenced by the impact inertia, the interfacial tensions and the liquid viscosity, which are similar inside and outside. The only difference is that during the fast-moving process of the contact line, it is inertia dominated outside while it is surface tension dominated inside. In both situations, it is expected that the relationship between the DCA and the contact line moving speed U_{cl} is applicable. So, it is reasonable to apply the DCA measured from the outside to mimic that inside the droplet. Figure 1 shows a schematic view of the apparatus we used to determine DCA. A water pump is used to pump water slowly with precisely controlled volume into a 26G syringe needle, and a pendant drop is generated with diameter of 2.6 ± 0.1 mm. The height between the needle to the substrate could be adjusted to determine the impact speed. The substrate used is a polished smooth silicon wafer with roughness lower than 1 nm and the SCA of the substrate is $\theta_s = 48.5^\circ \pm 2^\circ$. A video of the droplet spreading-receding process is supplied in Supplementary Material 1.

A high-speed camera iX-i SPEED 7, with a frame rate of 20000 fps at pixel of 952×672 , is used to capture high-resolution droplet dynamics. With the sharp outline of the droplet, image processing based on MATLAB platform is used to obtain contact line moving speed and contact angle. The error of contact line moving speed measurement is about ± 0.1 m/s and the error of the contact angle extracted is $\pm 2^\circ$. According to our experiment measurement, the maximum advancing contact angle during spreading is $\theta_a = 95^\circ$ and the minimum receding contact angle during retraction is $\theta_r = 5^\circ$. The dynamic contact angle measured as a function of contact line moving speed is shown in Fig.2, which could be well fitted by Yokoi's DCA model when the empirical parameter K_a is taken as 2×10^{-9} and K_r is taken as 2×10^{-8} . It should be noted here that in the DCA model shown in Fig.2, $\theta_s = 50^\circ$ rather than 48.5° is used to better describe Lee's experiments.

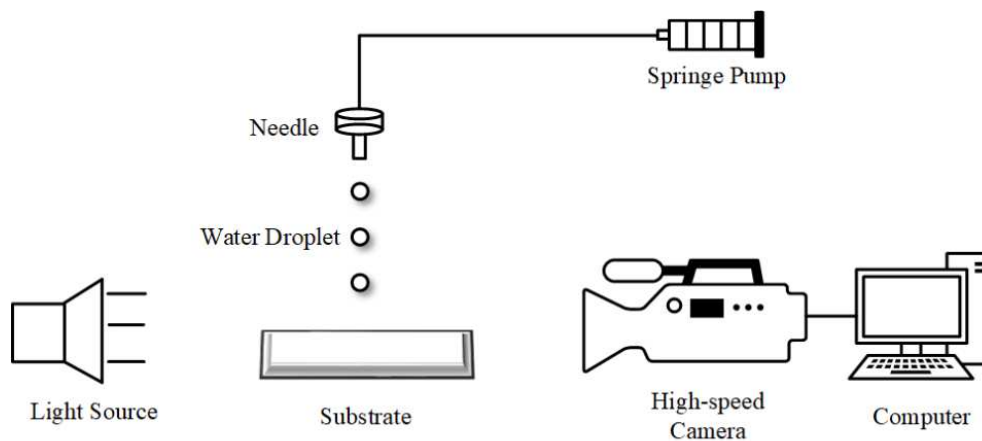


Figure 2 Experiment setup for dynamic contact angle measurement

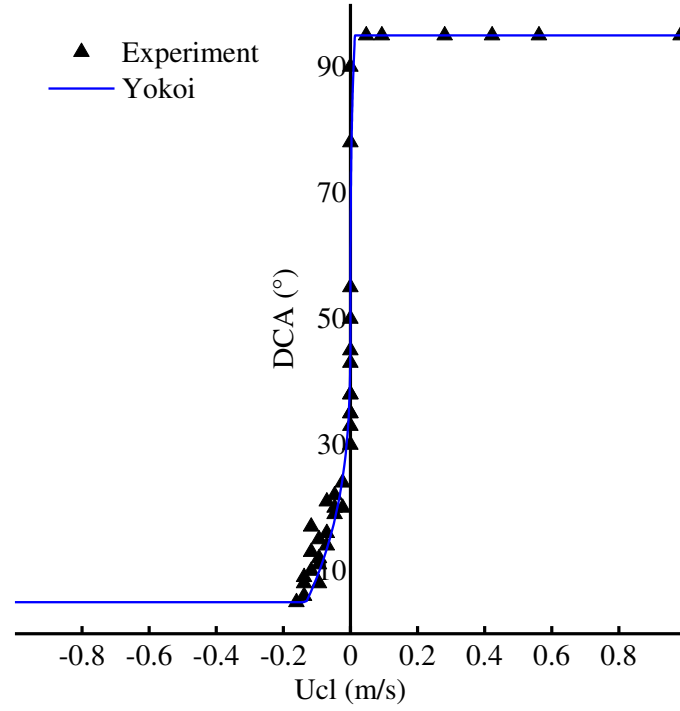


Figure 3 Dynamic contact angle (DCA) model fitted by Yokoi model

3. Results and discussion

3.1 Simulation of droplet impact dynamics

To validate the DCA model measured from the experiment, a phase field simulation of the droplet impact spreading and receding process is firstly conducted. The DCA model in Eq. 5 is used. As for the Cahn number of the phase field method, the value of $Cn=0.01$ by using $\varepsilon = 2.6 \mu m$ is used. Both the parameter χ and the slip length would influence the results dramatically. As summarized in ref [49], the slip length on hydrophilic glass substrates varies from 0 to $1 \mu m$ ⁴⁹, a cross analysis of the phase field mobility tuning parameter χ and slip length L_s is performed, as shown in Fig.4, where the spreading factor $\beta = D(t)/D_0$ is used to reflect simulation accuracy.

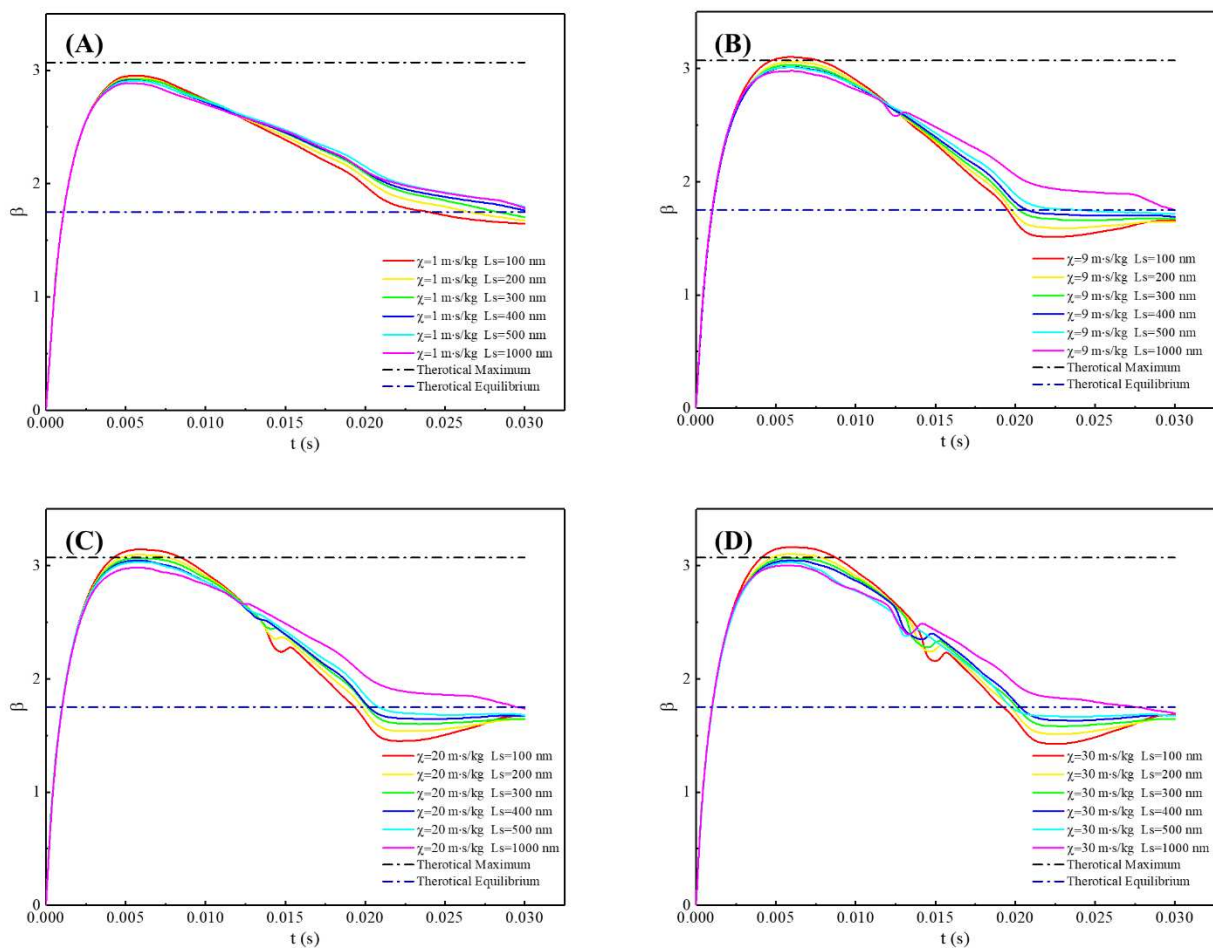
It turns out that when the χ is taken as $9 m \cdot s/kg$ and L_s is taken as $500 nm$, the simulation results agree best with experiment measurement as shown in Fig. 5 and Fig. 6. The comparison of maximum spreading factor β_{max} and equilibrium spreading factor β_e between experiment measurement/simulation results and theoretical results is shown in Table 1. The β_{max} is calculated by equation

$$\beta_{max} = \sqrt{\frac{We+12}{3(1-\cos\theta_a)+4(We/\sqrt{Re})}} \quad (6)$$

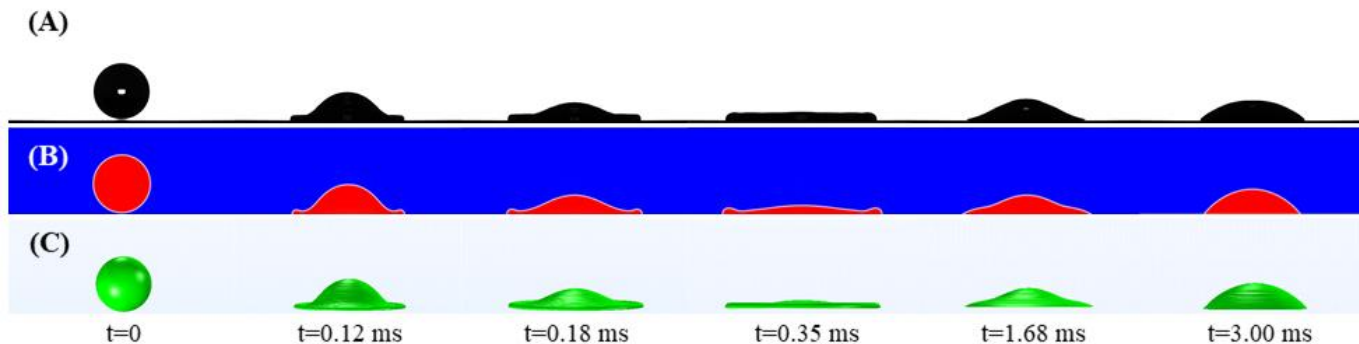
as proposed by Pasandideh-Fard⁴¹. The relative error between DCA simulation results and theoretical result is 1.95% for β_{max} and is 2.29% for β_e . It should be noted here that the relative error of β_e between experimental and theoretical results is because the SCA measured in the experiment is 48.5° while 50° is used in the theoretical calculation.

As shown in Fig.4, when the mobility tuning parameter χ is taken too small, such as $1 m \cdot s/kg$, the β_{max}

232 is lower than theoretical results and cannot reach an equilibrium state until 30 ms. This is because the diffusion
 233 of the interface is too weak to drive the interface moving at low Ca number situation when the inertia is well
 234 dissipated. While if the χ is taken too big, i.e., 30 m·s/kg, there is an obvious fluctuation during the
 235 retraction process at t=10-15 ms and that is because the diffusion dominates the system and imposes the droplet
 236 with extra kinetic energy transferred from surface energy. As for the influence of slip length, the smaller it is
 237 taken, the bigger β_{\max} is obtained, leading to more obvious fluctuation before reaching the equilibrium state,
 238 which is due to the lower friction from the substrate.



239 Figure 4 Influence of mobility tuning parameter χ and slip length L_s to the spreading factor
 240 (A) $\chi = 1$ m·s/kg (B) $\chi = 9$ m·s/kg (C) $\chi = 20$ m·s/kg (D) $\chi = 30$ m·s/kg
 241



242 Figure 5 Comparison of droplet impact spreading and receding process between simulation and experiment results
 243 (A) Experiment results (B) Two-dimensional view of simulation results (C) Three-dimensional view of simulation
 244 results
 245

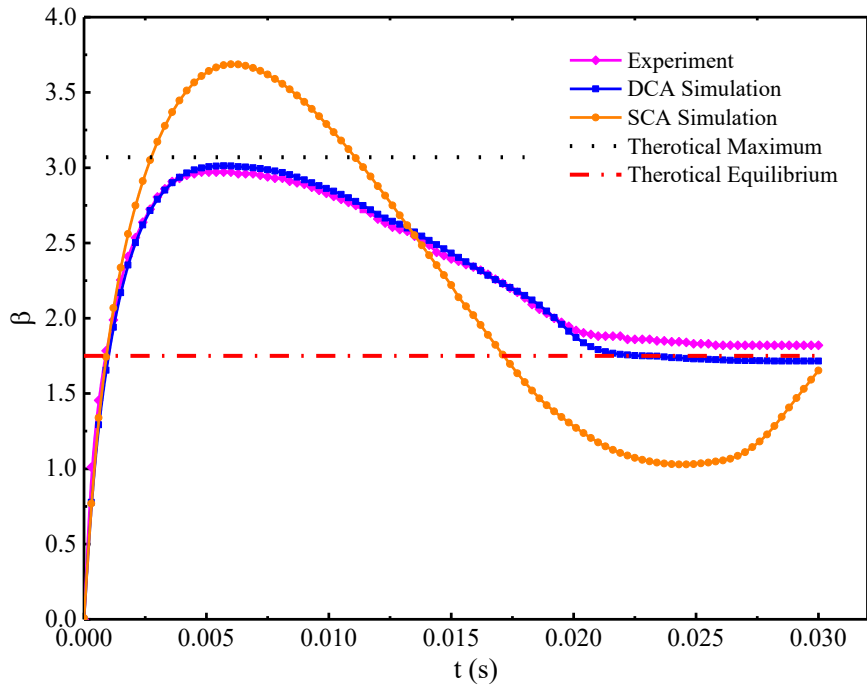


Figure 6 Comparison of β development with time between experiment, DCA simulation and SCA simulation results

Table 1 Comparison of β_{\max} and β_e between simulation & experiment results with theoretical results

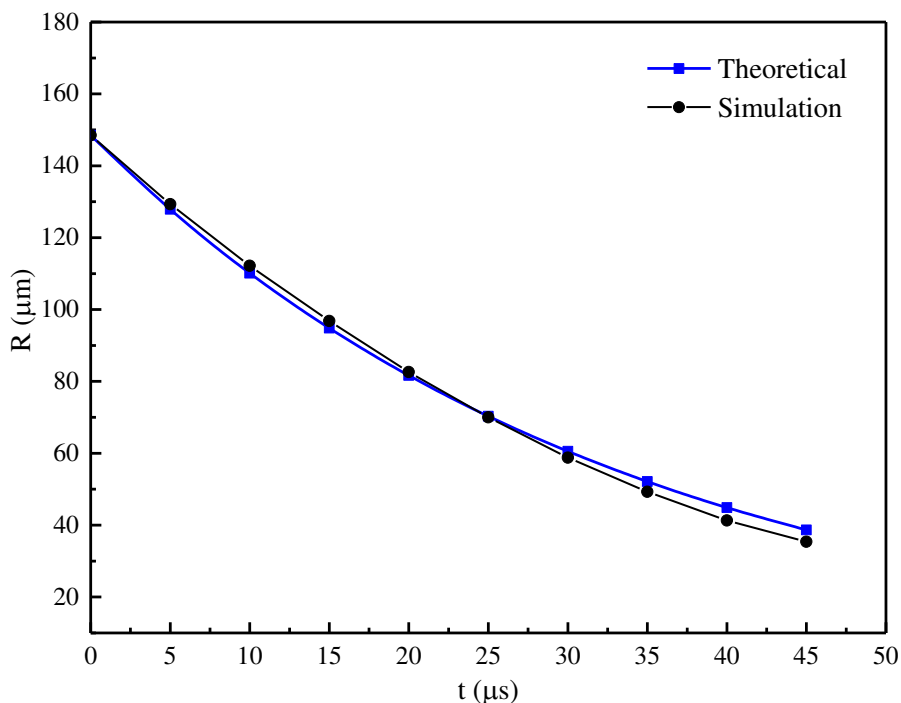
Item	Theoretical Results	Experiment Measurement	DCA Simulation Results	Relative Error of Experiment	Relative Error of DCA Simulation
β_{\max}	3.07	2.97	3.01	3.26%	1.95%
β_e	1.75	1.81	1.71	3.43%	2.29%

The comparisons in Fig.5 and Fig.6 show that the simulation agrees very well with the experimental data. The droplet firstly spreads fast during $t < 3.5 \text{ ms}$, driven by the strong impact inertia and then the contact line movement gradually decelerates. After reaching the maximum spreading factor β_{\max} at $t = 5.8 \text{ ms}$, the droplet recedes slowly under the control of surface tension and viscous force. At $t > 25 \text{ ms}$, the droplet deposits on the surface, characterized by a SCA. This shows that the PFM in combination of the DCA model can capture reliably the interface movement, and is adopted for further studies, as below.

3.2 Simulation of the entrapped air film evolution

With the well validated DCA model (i.e., Eq.5) and the slip length (i.e., $L_s = 500 \text{ nm}$), the simulation of entrapped air film evolution during droplet impact on a solid surface is conducted. As for the PFM parameters, the diameter of the final spherical bubble is used as the characteristic length of the system, which is around $50 \text{ }\mu\text{m}$, so the ε is set as 500 nm with the maximum mesh size $h_m = 500 \text{ nm}$ to make the $Cn = 0.01$. Since it is quite a different physical system both in size and time scale from the droplet impact spreading and receding process, $\chi = 9 \text{ m}\cdot\text{s}/\text{kg}$ found to best fit the outer simulation is no longer be feasible here. After testing χ ranging from 50 to 500 $\text{m}\cdot\text{s}/\text{kg}$, $\chi = 250 \text{ m}\cdot\text{s}/\text{kg}$ is chosen as the optimum values. The much higher χ value is because the entrapped air film dynamics is more controlled by surface tension than inertia.

265 The comparison between simulation results and theoretical predictions⁶ of the air film radius varying with
 266 time during retraction is shown in Fig. 7. It is found when χ is taken too small such as $50 \text{ m}\cdot\text{s}/\text{kg}$, the initial
 267 size of the air film is larger than the experimental results and when it is taken too large such as $350 \text{ m}\cdot\text{s}/\text{kg}$,
 268 the pinch off of the secondary daughter droplet is restrained because the advection is overly damped by the
 269 diffuse, as shown in Supplementary Material 2.



270

271

272 **Figure 7 Comparison between simulation result and theoretical prediction of the air film radius varying with time during retraction**

273

274

273 With $\chi = 250 \text{ m}\cdot\text{s}/\text{kg}$, the initial radius of the air film is $148.5 \mu\text{m}$ as compared to $145 \pm 5 \mu\text{m}$ in Lee's
 274 experiment, and the initial height of the air film (taken at water fraction $\Phi_w = 0.9$ in the interface) is 1.91
 275 μm , which agrees quite well with experimental observations in ref [6], i.e., $1.9 \mu\text{m}$ over a range of $We \sim (70-$
 276 $900)$ and $Re \sim (1600-5800)$.

277

278

279

280

281

282

283

284

285

286

287

277 As shown in Fig.8 and Supplementary Material 3, the droplet would firstly glide on the thin air film before
 278 contacting, and form a dimple shape at the bottom surface upon droplet wetting the substrate, resulting in the
 279 entrapment of an air film. The air film retracts rapidly by surface tension to minimum the surface energy at
 280 $t < 40.5 \mu\text{s}$, and at the same time a capillary wave transports inwards on the upper surface of the air film.
 281 After the trough of the capillary wave reaching the substrate at $t=47.9 \mu\text{s}$, the toroidal bubbles still keep
 282 contracting until converging at $t=58.9 \mu\text{s}$. A tiny secondary daughter droplet is then pinched off at $t=62.6 \mu\text{s}$
 283 at the center of the bubble and merges with the mother daughter droplet at $t=73.6 \mu\text{s}$. Finally, the spherical
 284 bubble stay attached to the substrate with a daughter droplet entrapped inside it. The volume ratio between the
 285 daughter droplet and the bubble V_d/V_b is 5.52% in our simulation, whereas the value is $5.2\% \pm 0.7\%$ in Lee's
 286 experiment. Such excellent agreement clearly shows that the combination of PFM and DCA can simulate
 287 accurately the air film dynamics upon droplet impact on a solid surface.

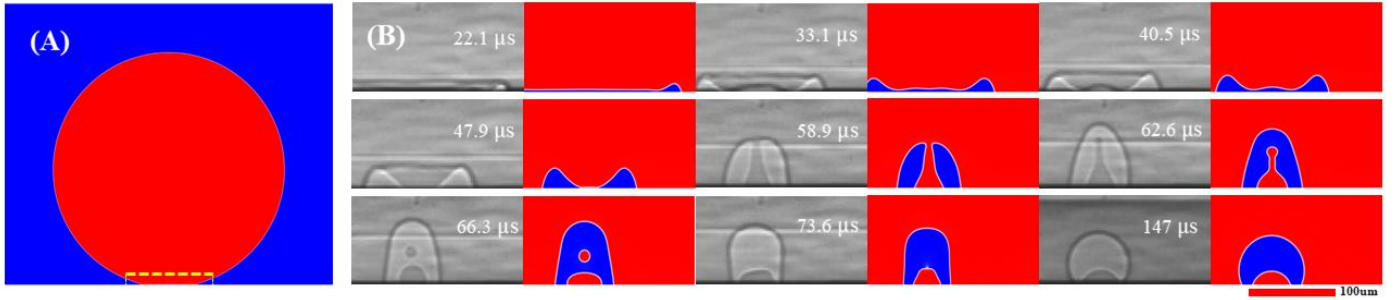


Figure 8 (A) Sketch of the entrapped air film evolution happening right after the droplet spreading begins.

(B) Comparison between Lee's experiment²² and our simulation results (liquid is denoted in red, while gas is denoted in blue). $D=2.6 \text{ mm}$, $U=1.25 \text{ m/s}$, $\rho = 996.4 \text{ kg/m}^3$, $\mu = 1.005 \text{ mPa} \cdot \text{s}$, $\sigma = 0.07275 \text{ N/m}$, $We=55.6$, $Re=3222$, $Oh=0.0023$

On the contrary, if the SCA model is used with $\theta = 50^\circ$, the toroidal bubble would leave the substrate between $t=55 \mu\text{s}$ and $65 \mu\text{s}$ before it converges, as shown in Fig.9. The result is quite similar to Kumar's simulation work, as shown in Fig xx²⁹, which is however inconsistent with the experimental observation²². Such an apparent difference can be ascribed by the mismatch between the contact angle model and the physical processes. As shown by both simulation and experiments, the retraction speed of the air film is very fast, i.e., as high as $\sim 5 \text{ m/s}$, the governing parameter to the interfacial dynamics should be the advancing contact angle, θ_a , rather than the SCA. If the contact angle model is inappropriately used, the values, even the direction of the interfacial forces, would be different, resulting in different simulation results.

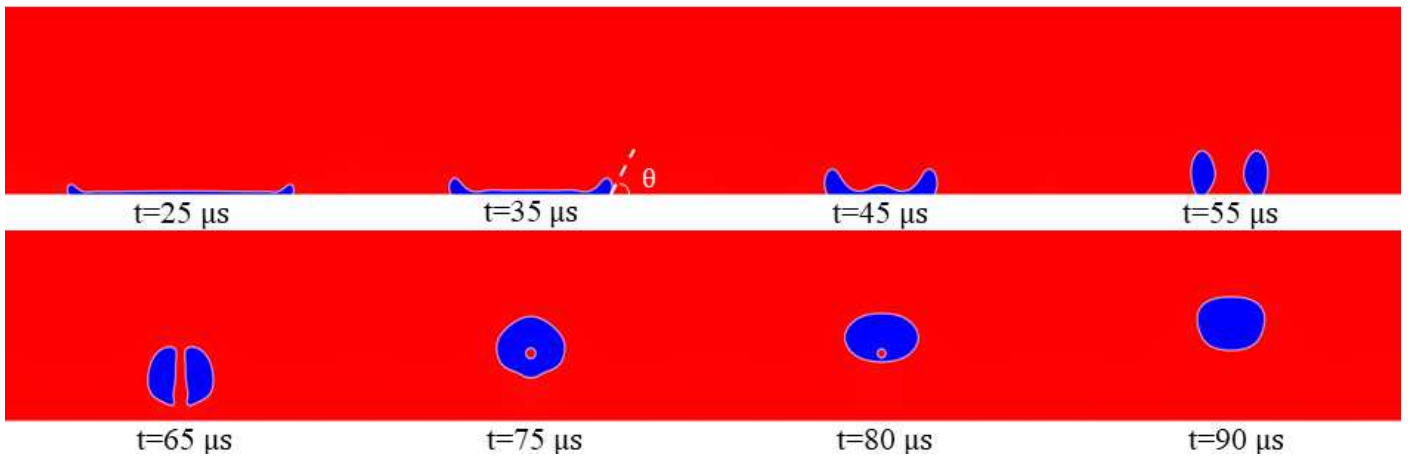


Figure 9 Simulation results with SCA model, $\theta = 50^\circ$

3.3 Effect of Oh number

After achieving the excellent agreement between our simulation and experimental results²², a parametric study of the influences of viscosity and surface tension of the droplet is conducted.

Fig.10 (A) shows the effect of droplet viscosity μ on the initial radius R_0 and the retraction process of the air film. As it shows, the initial radius increases from $148.5 \mu\text{m}$ to $210.1 \mu\text{m}$ when μ increases from $1 \text{ mPa} \cdot \text{s}$ to $5 \text{ mPa} \cdot \text{s}$. This agrees well with the experimental finding in ref [17] for inviscid or low-viscous fluids. As the time evolves, the air film shrinks due to the effect of surface tension in minimizing the area, and approaches asymptotically to an equilibrium value, which is only affected slightly by the viscosity. According our measurements, the maximum retraction speed is 4.24 m/s for $\mu = 1 \text{ mPa} \cdot \text{s}$ and 2.26 m/s for

$\mu = 5 \text{ mPa} \cdot \text{s}$ respectively. This agrees well with the air film retraction speed, described by Thoroddsen in ref [6]:

$$R(t) = R_0 \exp(-C\sqrt{\pi\sigma/\rho Vt}) \quad (7)$$

where V is the volume of the final spherical bubble and C is a system determined proportionality constant, which is proportional to $Oh^{-\frac{1}{2}} = \mu^{-\frac{1}{2}}(\rho\sigma D)^{\frac{1}{4}}$.

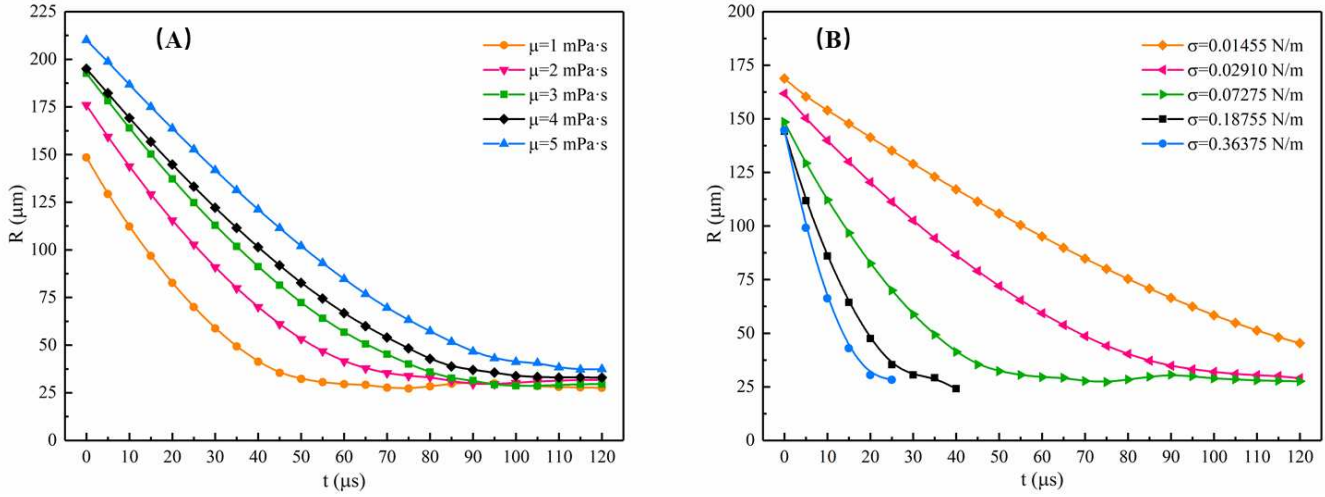


Figure 10 Influence of droplet viscosity and surface tension to the initial radius and retraction process of the air film

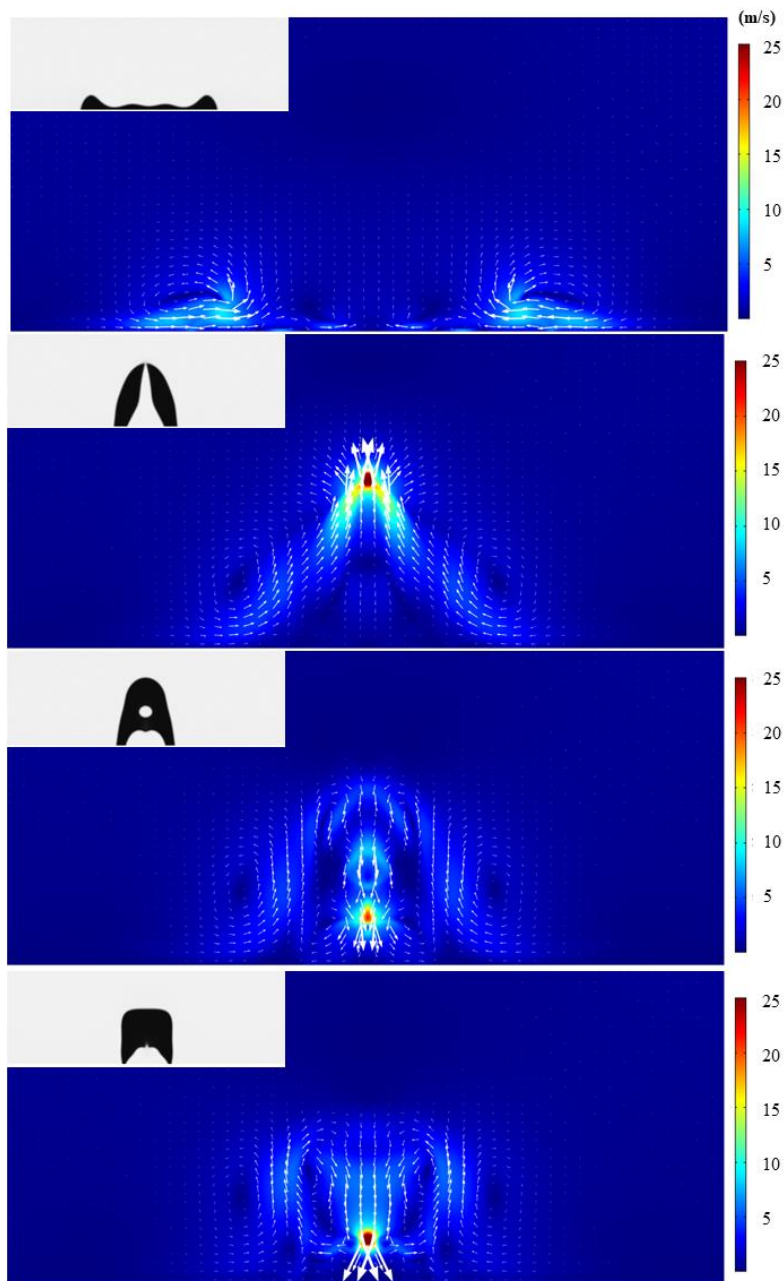
Fig.10 (B) illustrates the influence of surface tension σ to the initial radius R_0 and the retraction process of the air film. It clearly shows that while the surface tension affects the initial radius, it becomes more important in the air film dynamics and the evolution time. As σ increases from 0.01455 N/m to 0.36375 N/m ($0.2\sigma_0$ to $5\sigma_0$), R_0 decreases from $174.3 \mu\text{m}$ to $140.7 \mu\text{m}$, which could be attributed to the anti-deformation effect of the surface tension. As shown in Eq. (7), the retraction speed increases as the surface tension increases. The maximum retraction speed U_0 is observed to be as high as 9.1 m/s at $\sigma = 0.36375 \text{ N/m}$, which is 2.2 times that of $\sigma = 0.07275 \text{ N/m}$.

One interesting finding is that at high surface tension, such as $\sigma = 0.18755 \text{ N/m}$ and $\sigma = 0.36375 \text{ N/m}$, the life time of the air film is significantly shortened. The detachment of the bubble would occur right after the daughter droplet generation, resulting in the possibilities of forming different regimes. This can be explained by the competition between the retracting speed of the air film and the propagation speed of the capillary wave. As the retraction speed increased at higher surface tension, so does the propagation speed of the capillary wave. As described in ref [6] and [16], the travelling velocity of the wave could be estimated as:

$$c_g = 1.5\sqrt{2\pi\sigma/\rho\lambda} \quad (8)$$

where λ is the wavelength and it's $60 \mu\text{m}$ for $\sigma = 0.07275 \text{ N/m}$ and $30 \mu\text{m}$ for $\sigma = 0.36375 \text{ N/m}$, as obtained from our simulation. Consequently, the propagation speed of the capillary wave becomes 3.16 times faster when the tension increases from 0.07275 N/m to 0.36375 N/m . As a result, the trough of the wave would reach the substrate much earlier with much higher surface energy left, which promotes the

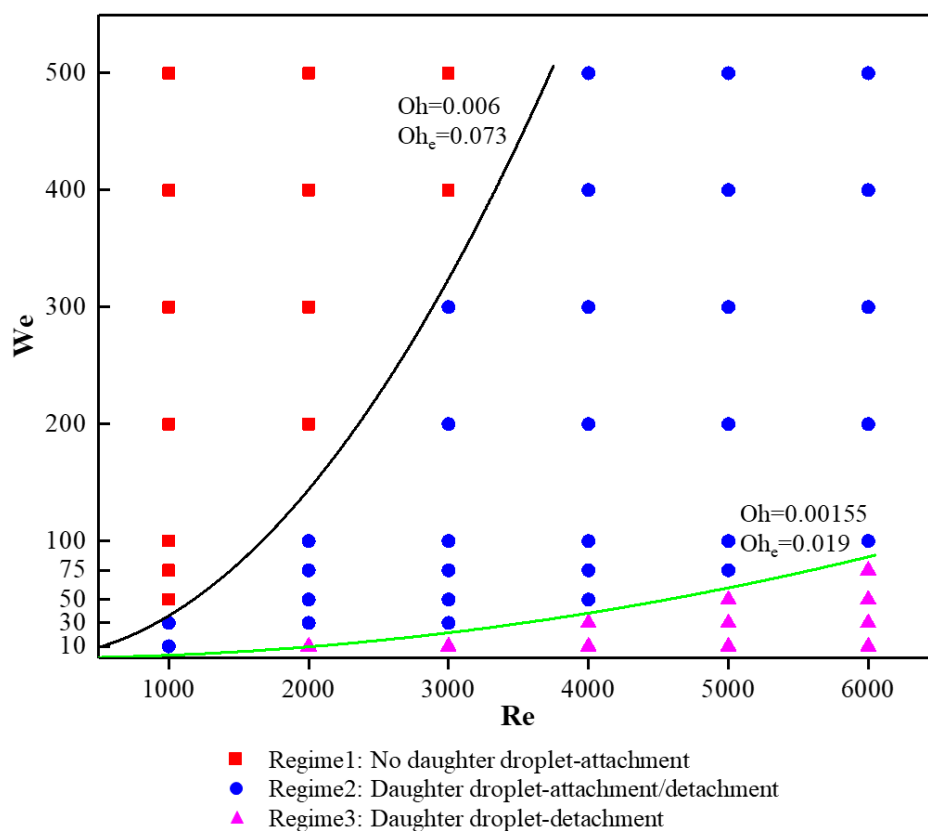
338 pinch off of secondary daughter droplet, and the subsequent fast contraction of the bubble-daughter surface.
 339 In addition, our simulation shows that there is a strong vortex street behind the rim of the air film generated
 340 by the faster retraction. On one side it pushes the toroidal bubble converging inwards with higher momentum,
 341 and at the other side, it results in an enhanced downstream flow inside the daughter droplet, which
 342 subsequently squeezes the daughter droplet out of the surrounding bubble, as shown in Fig.11. It should be
 343 noted here that the reason for the detachment of the air bubble by high surface tension is quite different from
 344 the SCA determined situation, as discussed in the next section.



345
 346 **Figure 11 Velocity Field with streamline for $\sigma=0.36375$ N/m, the arrow is proportional to velocity**

347 We further investigated the influence of Oh to the dynamics of the air film after the contraction, by varying
 348 viscosity and surface tension of the droplet while keep the droplet diameter, impact velocity and gas properties
 349 constant. The Weber number investigated ranges from 10-500, and the Reynolds number ranges from 1000-
 350 6000, leading to Oh ranges from 5.27×10^{-4} to 2.24×10^{-2} . At high Oh numbers, because of the viscous
 351 damping effects as reported by Lee²², the capillary wave could not reach the substrate to separate the air

352 volume into a toroidal shape, and no daughter droplet could be generated. While at low Oh number, the air
353 bubble always leaves the substrate due to the dominance of surface tension. From the simulation, it is revealed
354 that there are three possible scenarios at different Oh numbers: i) Regime 1: No daughter droplet-attachment,
355 ii) Regime2: Daughter droplet-attachment/detachment, and iii) Regime3: Daughter droplet-detachment, as
356 summarized in Fig. 12 and shown schematically in Fig. 13. Instead of the two previously reported regimes
357 (i.e., Regime 1 at high Oh number and Regime 2 at moderate Oh number), it is predicted numerically that
358 there shall have another regime exists: the daughter droplet can be generated but always detach from the
359 substrate, i.e. Regime 3. The threshold between regimes 1 and 2 is $Oh_1=0.006$ and between regimes 2 and 3 is
360 $Oh_2=0.00155$ respectively. If considering the lubrication effect of the air film by defining an effective Oh
361 number, i.e., $Oh_e = OhSt^{-\frac{1}{3}}$ as proposed by ref [28], the threshold of Oh_e would be 0.073 and 0.019
362 respectively to demarcate the regime 1 and 2, and regime 2 and 3. Compared with Oh, Oh_e takes the influence
363 of the air properties into account, and thus would be more suitable for defining the 3-regimes phase diagram.
364 Consequently, the entrapped air bubble behavior could be characterized by three regimes considering a wide
365 span of Oh numbers. The newly predicted Regime 3 is yet to revealed experimentally. **And it also should be
366 noted here that in Regime 2, whether the bubble will attach to or detach from the substrate is simultaneously
367 determined by the volume ratio V_d/V_b and the static contact angle θ_s which will be discussed in section 3.4.**



368
369

Figure 12 Phase Diagram of air bubble dynamics according to We-Re

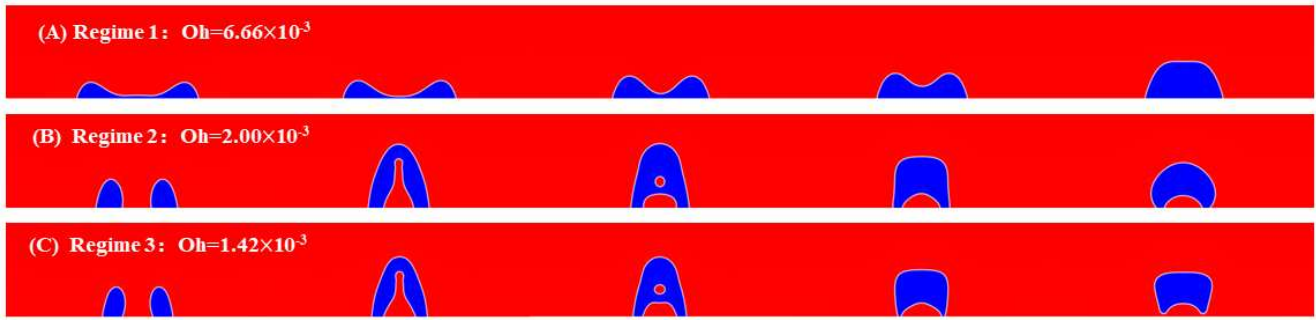


Figure 13 Exhibition of 3 regimes dependent on Oh number

3.4 Effect of dynamic contact angle to the V_d/V_b

For the moderate Oh or Oh_e regime, as has been discussed by Lee²², whether the bubble would detach from the substrate is determined by the SCA of the substrate. As the volume ratio of the daughter droplet to that to bubble, V_d/V_b , doesn't change with SCA, the more hydrophilic the surface is, the easier the air bubble detachment would happen. To better understand the mechanism, we measured the DCA of a highly hydrophilic silicon wafer, as shown by video 3 in in Supplementary Material 4. The SCA measured is 12° while the advancing contact angle is as high as 95° because it is the inertia-dominated process. For this substrate, the Ka in Yokoi DCA model is taken as 4×10^{-9} .

The simulation result with this DCA model, as shown in Fig.14, shows that after the daughter droplet is generated, the bubble finally detaches from the substrate at $t=90 \mu s$ which could be explained by the geometry relation shown in Fig.15 that at the given volume ratio of $V_d/V_b = 0.052$, the bubble would leave the substrate when the SCA is smaller than 42.5° .

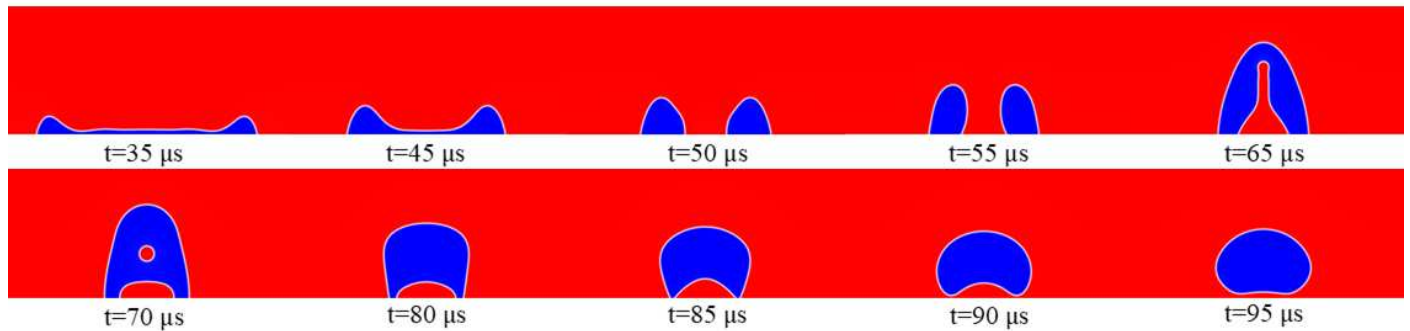


Figure 14 Bubble detaches from substrate at lower static contact angle, $\theta_s=12^\circ$

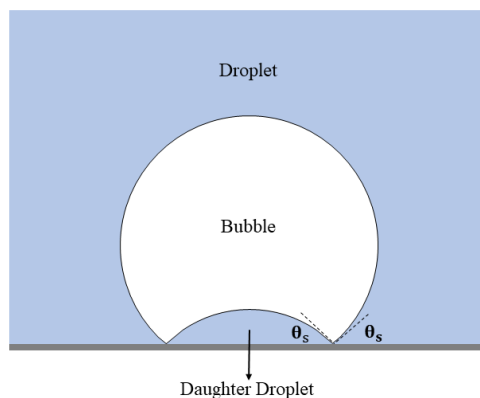
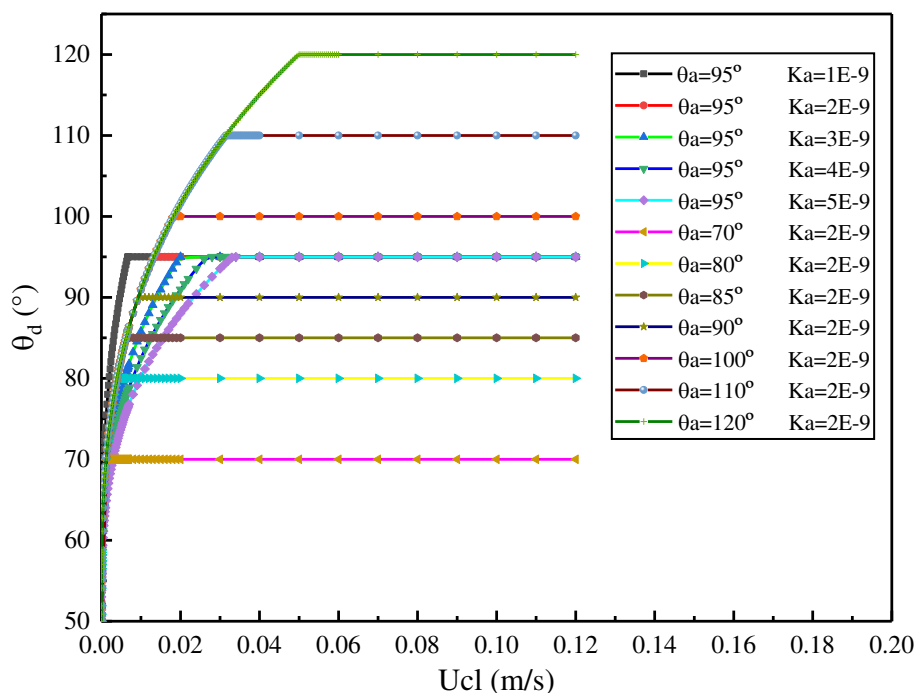


Figure 15 Geometrical relation of the critical case in SCA determined bubble attachment/detachment by Lee²²

389 This led us to think that it is the DCA that determines V_d/V_b . So, we studied the effect of θ_a and Ka in
390 the Yokoi DCA model on V_d/V_b with θ_a ranging from 70° to 120° for a given $Ka=2 \times 10^{-9}$, and Ka ranging
391 from 1×10^{-9} to 5×10^{-9} for a given $\theta_a = 95^\circ$, as shown in Fig.16. It should be noted here that since the air film
392 retraction corresponds to the droplet spreading, so the negative part of DCA models ($U_{cl} \leq 0$) isn't shown and
393 it would not cause any error. It turns out that the θ_a influences the volume ratio V_d/V_b negatively correlated
394 while V_d/V_b shows no regular and obvious variation with Ka , as shown in Table.2. This implies the advancing
395 contact angle θ_a plays an important role in determining V_d/V_b . However, it needs to be mentioned here that
396 the θ_a is simultaneously influenced by the impact inertia, liquid viscosity, surface tension and static contact,
397 and to the best of our knowledge, no explicit relationships among them has been achieved yet. For instance,
398 according to ref [35]-ref [41], the estimated increase of θ_a when droplet viscosity increases from $1 \text{ mPa} \cdot \text{s}$
399 to $10 \text{ mPa} \cdot \text{s}$ will be less than 10° and the influence of surface tension is in a reverse way but normally
400 weaker.



401
402
403
404
Figure 16 DCA Models with different θ_a and Ka

Table 2 Influence of θ_a and Ka in DCA model to V_d/V_b

θ_a ($^\circ$)	Ka	V_d/V_b (%)
70	$2 \cdot 10^{-9}$	Detachment
80	$2 \cdot 10^{-9}$	Detachment
85	$2 \cdot 10^{-9}$	6.35
90	$2 \cdot 10^{-9}$	5.97
95	$2 \cdot 10^{-9}$	5.52
100	$2 \cdot 10^{-9}$	5.34
110	$2 \cdot 10^{-9}$	3.76
120	$2 \cdot 10^{-9}$	2.16

θ_a (°)	Ka	V_d/V_b (%)
95	$1 \cdot 10^{-9}$	6.08
95	$2 \cdot 10^{-9}$	5.52
95	$3 \cdot 10^{-9}$	5.63
95	$4 \cdot 10^{-9}$	5.43
95	$5 \cdot 10^{-9}$	5.36

4. Conclusion

The droplet impact and dynamics of inner entrapped air film were numerically investigated achieved through Phase Field Method (PFM) by properly setting the mobility tuning parameter χ . And it's been proved by our simulations with 2 dynamic contact angle (DCA) models measured from our experiments (Substrate 1: $\theta_s \approx 50^\circ, \theta_a \approx 95^\circ$, Substrate 2: $\theta_s \approx 12^\circ, \theta_a \approx 95^\circ$) that the DCA model measured from the droplet impact spreading and receding process could and should be used to simulate the entrapped air film dynamics. The liquid viscosity and surface tension could significantly influence the initial radius and the retraction dynamics of the air film. More importantly, their competition would determine the bubble attachment/detachment regimes separated by the Oh_e number. Under high Oh_e regime, the bubble tends to attach to the substrate with no daughter generation due to high viscous dissipation of the capillary wave. While as we newly discovered, under low Oh_e regime, the bubble tends to detach from the substrate resulted from the strong downstream flow inside the bubble stirred by the vortex following the retraction, the energy comes from the high surface energy with low viscous dissipation. Under moderate Oh_e regime, whether the bubble will attach or detach from the substrate will be determined by the static contact angle given that the volume ratio V_d/V_b is determined by the advancing dynamic contact angle. Our finding about what happens at low Oh situation and the decisive role of advancing contact angle in determining V_d/V_b at moderate Oh regimes provides more comprehensive instructions to control entrapped air bubble attachment/detachment behavior in droplet impacting on a solid surface. At last, the χ tested by our investigation may provide references for one to simulate droplet impact dynamic or air entrapment dynamics with PFM.

Acknowledgement

This work was supported by Beijing Municipal Science and Technology Commission, National Natural Science Foundation of China (Grant No.11772034). Also thanks for the support of Integrated Projects utilizing the Space Environment on ISS and CSS supported by CMSA and ESA (TGMTYY00-RW-03).

433
434
435
436
437
438
439
440
441
442
443
444
445
446
447
448
449
450
451
452
453
454
455
456
457
458
459
460
461
462
463
464
465
466
467
468
469
470
471
472
473
474
475
476
477
478
479
480

References

1. A. L. Yarin, *Annu. Rev. Fluid Mech.* **38**, 159-192 (2006).
2. C. Josserand and S. T. Thoroddsen, *Annual review of fluid mechanics* **48**, 365-391 (2016).
3. H. Lambley, T. M. Schutzius and D. Poulikakos, *Proceedings of the National Academy of Sciences* **117** (44), 27188-27194 (2020).
4. P. Kant, R. B. Koldewij, K. Harth, M. A. van Limbeek and D. Lohse, *Proceedings of the National Academy of Sciences* **117** (6), 2788-2794 (2020).
5. S. Chandra and C. Avedisian, *Proceedings of the Royal Society of London. Series A: Mathematical and Physical Sciences* **432** (1884), 13-41 (1991).
6. S. Thoroddsen, T. Etoh, K. Takehara, N. Ootsuka and Y. Hatsuki, *Journal of Fluid Mechanics* **545**, 203 (2005).
7. P. D. Hicks and R. Purvis, *J Fluid Mech* **649**, 135-163 (2010).
8. W. Bouwhuis, R. C. van der Veen, T. Tran, D. L. Keij, K. G. Winkels, I. R. Peters, D. van der Meer, C. Sun, J. H. Snoeijer and D. Lohse, *Physical review letters* **109** (26), 264501 (2012).
9. S. Mandre, M. Mani and M. P. Brenner, *Physical review letters* **102** (13), 134502 (2009).
10. M. Mani, S. Mandre and M. P. Brenner, *Journal of Fluid Mechanics* **647** (1), 163-185 (2010).
11. E. Klaseboer, R. Manica and D. Y. Chan, *Physical review letters* **113** (19), 194501 (2014).
12. P. D. Hicks and R. Purvis, *Journal of Fluid Mechanics* **735**, 120-149 (2013).
13. J. de Rooter, J. M. Oh, D. van den Ende and F. Mugele, *Physical review letters* **108** (7), 074505 (2012).
14. Y. Liu, P. Tan and L. Xu, *Journal of Fluid Mechanics* **716** (2013).
15. L. Mahadevan, *Phys. Rev. Lett* **108** (7), 074503 (2012).
16. J. M. Kolinski, L. Mahadevan and S. Rubinstein, *EPL (Europhysics Letters)* **108** (2), 24001 (2014).
17. K. Langley, E. Li and S. T. Thoroddsen, *Journal of Fluid Mechanics* **813**, 647 (2017).
18. E. Q. Li, K. R. Langley, Y. S. Tian, P. D. Hicks and S. T. Thoroddsen, *Physical review letters* **119** (21), 214502 (2017).
19. K. R. Langley, E. Q. Li, I. U. Vakarelski and S. T. Thoroddsen, *Soft matter* **14** (37), 7586-7596 (2018).
20. K. Langley and S. T. Thoroddsen, *Journal of Fluid Mechanics* **878** (2019).
21. K. R. Langley, A. A. Castrejón-Pita and S. T. Thoroddsen, *Soft Matter* **16** (24), 5702-5710 (2020).
22. J. San Lee, B. M. Weon, J. H. Je and K. Fezzaa, *Physical review letters* **109** (20), 204501 (2012).
23. V. Mehdi-Nejad, J. Mostaghimi and S. Chandra, *Physics of fluids* **15** (1), 173-183 (2003).
24. W. Xiong and P. Cheng, *International Journal of Heat and Mass Transfer* **124**, 1262-1274 (2018).
25. F. Yeganehdoust, R. Attarzadeh, I. Karimfazli and A. Dolatabadi, *International Journal of Multiphase Flow* **124**, 103175 (2020).
26. Y. Guo, L. Wei, G. Liang and S. Shen, *International Communications in Heat and Mass Transfer* **53**, 26-33 (2014).
27. D. Li, D. Zhang, Z. Zheng and X. Tian, *International Journal of Heat and Mass Transfer* **115**, 186-193 (2017).
28. Z. Jian, M. A. Channa, A. Kherbeche, H. Chizari, S. T. Thoroddsen and M.-J. Thoraval, *Physical Review Letters* **124** (18), 184501 (2020).
29. R. Kumar, R. K. Shukla, A. Kumar and A. Kumar, *International Journal of Thermal Sciences* **153**, 106363 (2020).
30. J. W. Cahn and J. E. Hilliard, *The Journal of chemical physics* **28** (2), 258-267 (1958).
31. P. Yue, J. J. Feng, C. Liu and J. Shen, *Journal of Fluid Mechanics* **515**, 293 (2004).
32. Q. Zhang, T.-Z. Qian and X.-P. Wang, *Physics of Fluids* **28** (2), 022103 (2016).
33. C. Y. Lim and Y. C. Lam, *Microfluidics and nanofluidics* **17** (1), 131-148 (2014).
34. R. Zanella, G. Tegze, R. Le Tellier and H. Henry, *Physics of Fluids* **32** (12), 124115 (2020).
35. M. Shen, B. Q. Li, Q. Yang, Y. Bai, Y. Wang, S. Zhu, B. Zhao, T. Li and Y. Hu, *International Journal of Multiphase Flow* **116**, 51-66 (2019).
36. E. Gelissen, C. van der Geld, M. Baltussen and J. Kuerten, *International Journal of Multiphase Flow* **123**, 103173 (2020).
37. F. Bai, X. He, X. Yang, R. Zhou and C. Wang, *International Journal of Multiphase Flow* **93**, 130-141 (2017).
38. I. S. Bayer and C. M. Megaridis, *Journal of Fluid Mechanics* **558**, 415 (2006).
39. D. Vadillo, A. Soucemarianadin, C. Delattre and D. Roux, *Physics of fluids* **21** (12), 122002 (2009).
40. I. V. Roisman, R. Rioboo and C. Tropea, *Proceedings of the Royal Society of London. Series A: Mathematical, Physical*

481 and Engineering Sciences **458** (2022), 1411-1430 (2002).

482 41. M. Pasandideh-Fard, Y. Qiao, S. Chandra and J. Mostaghimi, *Physics of fluids* **8** (3), 650-659 (1996).

483 42. H. Almohammadi and A. Amirfazli, *Journal of colloid and interface science* **553**, 22-30 (2019).

484 43. R. Rioboo, M. Marengo and C. Tropea, *Experiments in fluids* **33** (1), 112-124 (2002).

485 44. C. Lam, R. Ko, L. Yu, A. Ng, D. Li, M. Hair and A. Neumann, *Journal of Colloid and Interface Science* **243** (1), 208-
486 218 (2001).

487 45. M. A. Quetzeri-Santiago, A. A. Castrejón-Pita and J. R. Castrejón-Pita, *Scientific reports* **9** (1), 1-10 (2019).

488 46. T. Xavier, D. Zuzio, M. Averseng and J.-L. Estivalezes, *Meccanica* **55** (2), 387-401 (2020).

489 47. Y. D. Shikhmurzaev, *Journal of Fluid Mechanics* **334**, 211-249 (1997).

490 48. K. Yokoi, D. Vadillo, J. Hinch and I. Hutchings, *Physics of Fluids* **21** (7), 072102 (2009).

491 49. C. Cottin-Bizonne, S. Jurine, J. Baudry, J. Crassous, F. Restagno and E. Charlaix, *The European Physical Journal E* **9**
492 (1), 47-53 (2002).

493

494

495

496

497

498

499

500

501

502

503

504

505

506

507

508

509

510

511

512

513

514

515

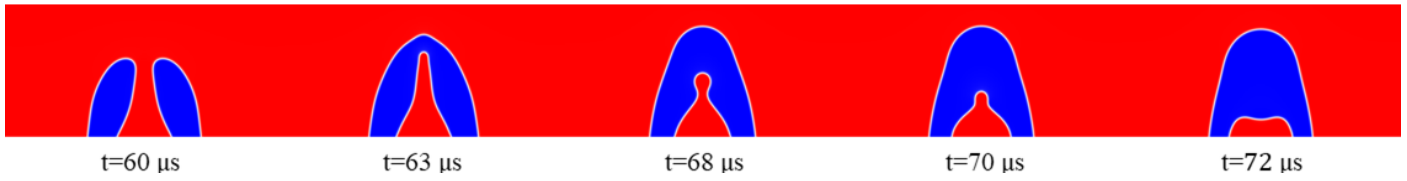
516

517

518 **Supplementary Materials**

519 **1. See Video 1.**

520 **2. Entrapped air film dynamics simulation with $\chi = 350 \text{ m} \cdot \text{s}/\text{kg}$, no pinch off of the secondary daughter**
521 **droplet.**



523 **3. See Video 2.**

524 **4. See Video 3.**